Highly rarefied gas flow through a right-angled micro-corner

D. Ben-Adva and A. Manela
Faculty of Aerospace Engineering, Technion - Israel Institute of Technology Haifa 32000, Israel

(Received 19 July 2024; accepted 3 December 2024; published 23 December 2024)

We study the two-dimensional steady flow of a highly rarefied gas through a right-angled corner element. Driven by an external pressure gradient, the free-molecular regime is analyzed for both diffuse and specular reflecting surfaces, and the solutions are validated through comparisons with direct simulation Monte Carlo calculations at finite Knudsen numbers. Imposing the pressure gradient through differences in the densities and temperatures of the gas reservoirs connected to the channel inlet and outlet, the results for the density- and temperature-drop-driven flows are analyzed and contrasted. The characteristic differences between the diffuse- and specular-wall-system flows, indicating sharper flow gradients and higher flow velocities in the latter, are rationalized. Closed-form expressions for the mass flow rate through the corner are derived, indicating a decrease of more than 40% in its mass transfer permeability due to the bend, compared with a straight channel configuration.

DOI: 10.1103/PhysRevFluids.9.123401

I. INTRODUCTION

Long-lasting interest in the field of micro-electro-mechanical systems (MEMS) has led to a large number of investigations on microfluidic flows, ubiquitously found in small-scale devices containing microchannel configurations [1,2]. Motivated by the ever-increasing complexity of channels' networks in microfluidic chips [3], the study of heat and mass transfer phenomena in irregular channel geometries has become the focus of numerous works. Within the context of rarefied gas flows, these have included investigations on the effects of channels' curvature [4], gradual section expansion [5–8], and other sudden cross-section variations [9–14], on the gas flow field.

Considering the impact of channel non-straightness, the flow in bent-wall configurations has been investigated and reviewed [15]. A sequence of numerical and experimental studies examined the problem in the continuum limit of small Knudsen numbers, considering single and multicurved setups [16–19]. Here, the numerical calculations were performed based on a Navier-Stokes-Fourier slip-flow model, applying either in-house [17] or commercial [18,19] solvers for the analysis. The study of the problem at arbitrary (and particularly non-small) rarefaction rates required the application of other models and numerical schemes. To this end, White *et al.* [20] used the direct simulation Monte Carlo (DSMC) method to study the flow through a T-junction double-bend microchannel configuration. Liu *et al.* [21] considered the Bhatnager-Gross-Krook (BGK) kinetic equation to investigate the effect of microbend geometry on the occurrence of the Knudsen minimum at non-small Knudsen numbers. More recently, Ho *et al.* [22] applied the Shakhov model to investigate the effect of gas rarefaction on flow detachment in microchannels with bends, establishing that flow separation is limited to relatively small Knudsen numbers. The three-dimensional flow through right-angled channels was investigated by Rovenskaya [23], using the Navier-Stokes-Fourier equations, and by Kulkarni *et al.* [24], applying the DSMC scheme.

Invariably, all of the above studies are based on numerical computations. As such, their scope is limited by the drawbacks of the numerical method applied and may benefit from direct analysis of the kinetic model. Yet, such analysis is formidably challenging at arbitrary rarefaction rates,

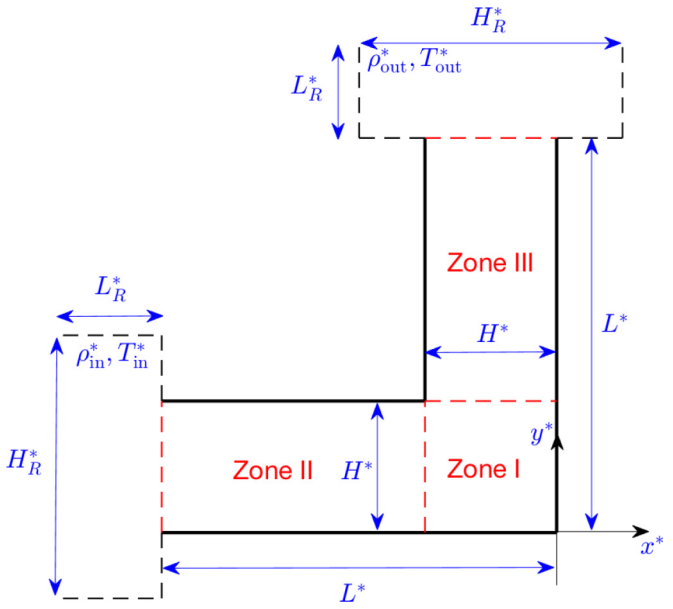

FIG. 1. Schematic of the problem. A two-dimensional right-angled corner of length $2L^*$ and width H^* is placed between inlet and outlet reservoirs, of sizes $L_R^* \times H_R^*$, with far-field densities ρ_{in}^* and ρ_{out}^*, and temperatures T_{in}^* and T_{out}^*, respectively. The outer corner is located at the axes $(x^*, y^*) = (0, 0)$ origin and the inner corner point is at $(x^*, y^*) = (-H^*, H^*)$. Zones I, II, and III are delineated by the dashed red lines for later discussion of the free-molecular gas flow kinematics in Sec. III.

even in the two-dimensional case, involving the consideration of the full Boltzmann equation or its model counterparts. While previous studies have focused on the low-Knudsen limit of the problem, the practical relevance of rigorously analyzing highly rarefied microchannel flows in bent-wall configurations is clear, and has not been addressed hitherto.

In view of the above, the objective of the present work is to investigate the two-dimensional gas flow through a right-angled corner at highly rarefied conditions. In line with common design constraints [3], the significance of such a study for the analysis and prediction of microchannels' network permeability is evident. We focus on the free-molecular limit, where the collisionless Boltzmann equation is considered and closed-form expressions for the gas mass flow rate through the channel are obtained. Depending on the channel walls' conditions and inlet and outlet section states, the flow field is examined in detail to shed light on the impact of geometrical bend on the channel mechanical performance. The ballistic-flow results are compared with DSMC predictions to test their accuracy and examine the breakdown of the collisionless regime with decreasing rarefaction rate. Notably, it is found that the free-molecular description remains valid through $O(1)$ Knudsen numbers.

In the next section, the problem is stated. The free-molecular limit is considered in Sec. III, where the cases of specular- and diffuse-wall systems are analyzed. The application of the DSMC scheme is discussed in Sec. IV, followed by the presentation of our results in Sec. V. The work conclusions are given in Sec. VI, and technical details are relegated to the Appendixes.

II. STATEMENT OF THE PROBLEM

A schematic of the problem is given in Fig. 1. Consider a perfect monatomic gas passing through a two-dimensional channel with a right-angled bend and a uniform width H^* (hereafter, asterisks denote dimensional quantities). Both x^*- and y^*-channel lengths are equal to L^*. The axes' origin is

set at the channel's outer corner point, such that its inner bend is located at $(x^*, y^*) = (-H^*, H^*)$. In the framework of gas kinetic theory and the present two-dimensional steady-flow setup, the problem is governed by the probability density function $f^* = f^*(x^*, y^*, \boldsymbol{\xi}^*)$ of finding a gas molecule at position (x^*, y^*) with a molecular velocity about $\boldsymbol{\xi}^* = (\xi_x^*, \xi_y^*, \xi_z^*)$. The inlet and outlet channel sections are connected to far-field equilibrium reservoirs, where the gas is maintained at uniform density and temperature, denoted by $(\rho_{\text{in}}^*, T_{\text{in}}^*)$ and $(\rho_{\text{out}}^*, T_{\text{out}}^*)$, respectively. At free-molecular conditions, gas particles entering the inlet (at $x^* = -L^*$, with $\xi_x^* > 0$) and outlet (along $y^* = L^*$, with $\xi_y^* < 0$) sections are unaffected by outcoming particles and are therefore distributed according to their equilibrium distributions

$$f_{\text{in}}^*(\xi_x^* > 0) = \frac{\rho_{\text{in}}^*}{\pi^{3/2} U_{\text{mp}_{\text{in}}}^{*3}} \exp\left[-\frac{\xi^{*2}}{U_{\text{mp}_{\text{in}}}^{*2}}\right] \quad \text{and} \quad f_{\text{out}}^*(\xi_y^* < 0) = \frac{\rho_{\text{out}}^*}{\pi^{3/2} U_{\text{mp}_{\text{out}}}^{*3}} \exp\left[-\frac{\xi^{*2}}{U_{\text{mp}_{\text{out}}}^{*2}}\right], \quad (1)$$

respectively. In Eq. (1), $U_{\text{mp}_{\text{in/out}}}^* = (2\mathcal{R}^* T_{\text{in/out}}^*)^{1/2}$ denotes the most probable speed of a gas particle at the inlet/outlet reservoir conditions, respectively, where $\mathcal{R}^*$ is the specific gas constant. While the above conditions are exact in the free-molecular regime (where the effect of channel outgoing particles on the reservoirs vanishes), they should be amended at finite flow rarefaction rates, due to possible interactions between incoming and outcoming particles at the channel end sections. Previous analyses of these amendments have resulted in a required effective change in the channel length at finite Knudsen numbers to mimic end-effect deviations [25–27]. These studies seek to find the effective length of the channel so that a one-dimensional linearly-fitted pressure profile mimics the imposed overall pressure difference between the reservoirs. To inspect this effect numerically in the near-free-molecular regime, extensive simulations of the problem should be carried out, taking into account the flow developed inside the inlet and outlet reservoirs. Such an effort was followed previously in various contexts, as illustrated, e.g., in the case of microchannel flow over a step [28]. Adopting a similar approach, we shall simulate the setup depicted in Fig. 1, including the reservoir domain, as discussed in Appendix C. Our findings support the expected insignificant impact of reservoir particle collisions on the flow inside the channel at near-free-molecular conditions. Consequently, we apply Eq. (1) hereafter as a viable approximation, which considerably facilitates the analysis and discussion.

Considering gas-surface interactions of the gas particles with the channel boundaries, we apply the Maxwell boundary condition [29]

$$f^*(x_b^*, y_b^*, \boldsymbol{\xi}^* \cdot \hat{\mathbf{n}} > 0) = \alpha \frac{\rho_b^*(x_b^*, y_b^*)}{\pi^{3/2} U_{\text{mp}_b}^{*3}} \exp\left[-\frac{\xi^{*2}}{U_{\text{mp}_b}^{*2}}\right] + (1-\alpha) f^*(x_b^*, y_b^*, \boldsymbol{\xi}^* - 2(\boldsymbol{\xi}^* \cdot \hat{\mathbf{n}})\hat{\mathbf{n}}), \quad (2)$$

where the relative α and $(1-\alpha)$ parts of the gas molecules are emitted diffusely and specularly, respectively, at each point (x_b^*, y_b^*) along the boundaries. Here, $\hat{\mathbf{n}}$ is a unit vector normal to the wall and into the channel and $\rho_b^*(x_b^*, y_b^*)$ is an unknown function associated with the mass flux of particles reflected from the boundary, to be determined below. Additionally, $U_{\text{mp}_b}^* = (2\mathcal{R}^* T_b^*)^{1/2}$ denotes the most probable speed of a gas particle at the channel wall temperature. We hereafter assume, for the diffuse-wall part, that the channel surfaces are isothermal and maintained at the inlet reservoir temperature, thus $U_{\text{mp}_b}^* = U_{\text{mp}_{\text{in}}}^*$. In practice, diffuse scattering occurs over rough surfaces, where the colliding particles attain thermal equilibrium with the reflecting wall. Specular interactions take place where the incident molecules collide with a solid surface and rebound elastically as if hitting a perfectly smooth wall. While none of these idealized scenarios exists in reality, it is commonly accepted that wall reflections from realistic surfaces may be described as a combination of diffuse and specular interactions, as formulated in Eq. (2).

To render the problem dimensionless, we scale the position by the channel width H^*, the velocity by the inlet's most probable molecular speed $U_{\text{mp}_{\text{in}}}^*$, and the density and temperature by ρ_{in}^* and T_{in}^*, respectively. The system's non-dimensional description is then governed by the channel's reduced geometrical half-length L, together with the outlet scaled density ρ_{out} and temperature T_{out}. In what

follows, we first analyze the free-molecular flow field through the micro-corner. Assuming steady flow conditions, the cases of specular and diffuse wall reflections are considered separately. No restrictions are made on the values of ρ_{out} and T_{out}, allowing for the inspection of the flow field at arbitrary pressure differences between the channel inlet and outlet reservoirs. The free-molecular analysis is followed by a description of the DSMC calculations carried out at non-infinite Knudsen numbers. Using the channel width as the characteristic length scale, the Knudsen number is given by

$$\text{Kn} = \lambda^*/H^*, \tag{3}$$

where λ^* marks the mean free path of a gas molecule. Assuming a hard-sphere gas model and basing our scaling on the inlet-reservoir conditions, $\lambda^* = m^*/(2^{1/2}\pi\rho^*_{\text{in}}d^{*2})$, where m^* and d^* denote the gas molecular mass and diameter, respectively [29].

III. THE FREE-MOLECULAR LIMIT

Assuming $\text{Kn} \to \infty$, the kinetic problem is governed by the collisionless two-dimensional steady Boltzmann equation

$$\xi_x\frac{\partial f}{\partial x} + \xi_y\frac{\partial f}{\partial y} = 0, \tag{4}$$

stating that $f(x, y, \boldsymbol{\xi})$ remains unchanged along "free-flight" particle trajectories in the absence of molecular collisions. Variations in the probability density function may therefore occur solely due to particle-surface interactions, prescribed by the scaled form of Eq. (2),

$$f(x_b, y_b, \boldsymbol{\xi}\cdot\hat{\mathbf{n}} > 0) = \alpha\frac{\rho_b(x_b, y_b)}{\pi^{3/2}}\exp\left[-\xi^2\right] + (1-\alpha)f(x_b, y_b, \boldsymbol{\xi} - 2(\boldsymbol{\xi}\cdot\hat{\mathbf{n}})\hat{\mathbf{n}}). \tag{5}$$

The solid wall condition in Eq. (5) is supplemented by the nondimensional counterpart of Eq. (1), prescribing the inlet and outlet section conditions

$$f_{\text{in}}(\xi_x > 0) = \frac{1}{\pi^{3/2}}\exp[-\xi^2] \quad \text{and} \quad f_{\text{out}}(\xi_y < 0) = \frac{\rho_{\text{out}}}{\pi^{3/2}T_{\text{out}}^{3/2}}\exp\left[-\frac{\xi^2}{T_{\text{out}}}\right], \tag{6}$$

respectively.

In what follows, the problem in Eqs. (4)–(6) is analyzed separately for the cases of fully specular ($\alpha = 0$, Sec. III A) and fully diffuse ($\alpha = 1$, Sec. III B) channels. Once the probability density function has been determined, the hydrodynamic fields are calculated via appropriate quadratures over the molecular velocity space [29]. Specifically, the density ρ, x- and y-velocity components, and normal stresses are given by

$$\rho = \int_{-\infty}^{\infty} f\,\mathrm{d}\boldsymbol{\xi} \quad u_x = \frac{1}{\rho}\int_{-\infty}^{\infty}\xi_x f\,\mathrm{d}\boldsymbol{\xi} \quad u_y = \frac{1}{\rho}\int_{-\infty}^{\infty}\xi_y f\,\mathrm{d}\boldsymbol{\xi}$$

$$P_{xx} = 2\int_{-\infty}^{\infty}(\xi_x - u_x)^2 f\,\mathrm{d}\boldsymbol{\xi} \quad P_{yy} = 2\int_{-\infty}^{\infty}(\xi_y - u_y)^2 f\,\mathrm{d}\boldsymbol{\xi} \quad \text{and} \quad P_{zz} = 2\int_{-\infty}^{\infty}\xi_z^2 f\,\mathrm{d}\boldsymbol{\xi}, \tag{7}$$

respectively, where $\mathrm{d}\boldsymbol{\xi} = \mathrm{d}\xi_x\mathrm{d}\xi_y\mathrm{d}\xi_z$. The pressure and temperature are computed via $p = (P_{xx} + P_{yy} + P_{zz})/3$ and the scaled form of the ideal-gas equation of state, $T = p/\rho$, respectively. Note that the solution in a combined specular-diffuse ($\alpha \neq 0, 1$) setup is obtained through linear superposition of the specular- and diffuse-wall probability density functions and substitution into Eq. (7). These cases are not considered hereafter, as the discussion of the $\alpha = 0$ and $\alpha = 1$ limits suffices for capturing the overall system behavior.

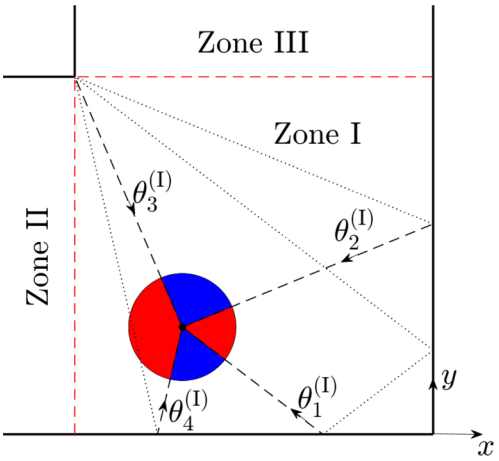

FIG. 2. Division of zone I for a specularly reflecting channel into sections of particles arriving from the inlet (red) or outlet (blue) reservoirs at the indicated location $(x_p, y_p) = (-0.7, 0.3)$. The black dashed and dotted lines combine ballistic trajectories of particles passing through the inner corner point $(-1, 1)$ and separating between sections of inlet- and outlet-originating particles. The $\theta_i^{(\mathrm{I})}$ $(i = 1, \ldots, 4)$ values pertain to the angles specified in Eq. (9), associated with the marked trajectories' directions.

A. Specular reflecting walls ($\alpha = 0$)

Considering a specular-wall channel, the impermeability condition is satisfied identically due to the symmetric form of the boundary condition [see Eq. (5) with $\alpha = 0$]. The particles in the channel may acquire either the inlet or outlet reservoir distributions [see Eq. (6)], and the problem solution reduces to sorting, at each (x, y) location, between f_{in} and f_{out}, based on the in-plane direction of the particle velocity vector

$$\theta = \arctan(\xi_y/\xi_x). \tag{8}$$

For clarity of presentation, we make use of the division of the channel domain into zones I, II and III, as marked in Fig. 1, and discuss particles' kinematics in each zone separately. Starting with zone I, located in the corner proximity and bounded by $x = -1$ and $y = 1$, the θ-sorting at a given location is determined by the line trajectories connecting the point of interest (x_p, y_p) with the inner corner location $(-1, 1)$. This is illustrated in Fig. 2 for $(x_p, y_p) = (-0.7, 0.3)$. Denoting

$$\theta_1^{(\mathrm{I})} = \arctan\left(\frac{y_p+1}{x_p-1}\right)+\pi, \quad \theta_2^{(\mathrm{I})} = \arctan\left(\frac{y_p-1}{x_p-1}\right)+\pi,$$
$$\theta_3^{(\mathrm{I})} = \arctan\left(\frac{y_p-1}{x_p+1}\right)+2\pi \quad \text{and} \quad \theta_4^{(\mathrm{I})} = \arctan\left(\frac{y_p+1}{x_p+1}\right), \tag{9}$$

we find that

$$f = \begin{cases} f_{\mathrm{in}}, & \theta_1^{(\mathrm{I})} < \theta < \theta_2^{(\mathrm{I})} \ \vee \ \theta_3^{(\mathrm{I})} < \theta < 2\pi \ \vee \ 0 < \theta < \theta_4^{(\mathrm{I})} \\ f_{\mathrm{out}}, & \theta_2^{(\mathrm{I})} < \theta < \theta_3^{(\mathrm{I})} \ \vee \ \theta_4^{(\mathrm{I})} < \theta < \theta_1^{(\mathrm{I})}. \end{cases} \tag{10}$$

Traversing to zone II, the sorting between inlet and outlet incoming particles becomes more complex in detail, yet similar in principle. Invariably, $f = f_{\mathrm{in}}$ for particles with $0 < \theta < \pi/2$ or $3\pi/2 < \theta < 2\pi$, while $f = f_{\mathrm{out}}$ for $\pi/2 < \theta < 3\pi/4$ or $5\pi/4 < \theta < 3\pi/2$. Within the $3\pi/4 < \theta < 5\pi/4$ interval, the trajectories separating between inlet and outlet particles are those arriving at the point of interest after intersecting the inner corner $(-1, 1)$, as presented in Fig. 3 for $(x_p, y_p) =$

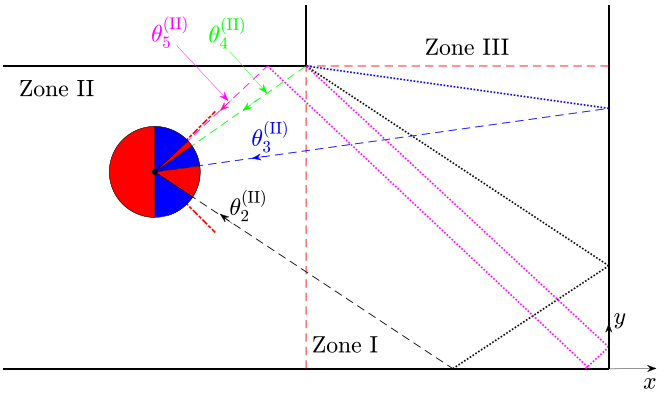

FIG. 3. Division of zone II of a specularly reflecting channel into sections of particles arriving from the inlet (red) or outlet (blue) reservoirs at the indicated location $(x_p, y_p) = (-1.5, 0.65)$. As explained in the text, $f = f_{\mathrm{in}}$ for particles with $0 < \theta < \pi/2$ or $3\pi/2 < \theta < 2\pi$, whereas $f = f_{\mathrm{out}}$ for $\pi/2 < \theta < 3\pi/4$ and $5\pi/4 < \theta < 3\pi/2$. Within $3\pi/4 < \theta < 5\pi/4$ (confined by the short red dash-dotted lines), particle sorting is specified by Eqs. (11) and (12). All trajectories, combined by dashed and dotted lines, are followed from the inner edge point $(-1, 1)$. The $\theta_i^{(\mathrm{II})}$ $(i = 2, \ldots, 5)$ values pertain to the angles specified in Eq. (11), associated with the marked trajectories directions, where $n = 1$ in $\theta_2^{(\mathrm{II})}(n)$ (in black) and $\theta_5^{(\mathrm{II})}(n)$ (in magenta).

$(-1.5, 0.65)$. Specifically, denoting

$$\theta_1^{(\mathrm{II})}(n) = \arctan\left(\frac{y_p + (2n-1)}{x_p + 1}\right) + \pi, \quad \theta_2^{(\mathrm{II})}(n) = \arctan\left(\frac{y_p + (2n-1)}{x_p - 1}\right) + \pi,$$
$$\theta_3^{(\mathrm{II})} = \arctan\left(\frac{y_p - 1}{x_p - 1}\right) + \pi, \quad \theta_4^{(\mathrm{II})} = \arctan\left(\frac{y_p - 1}{x_p + 1}\right) + \pi,$$
$$\theta_5^{(\mathrm{II})}(n) = \arctan\left(\frac{y_p - (2n+1)}{x_p - 1}\right) + \pi \quad \text{and} \quad \theta_6^{(\mathrm{II})}(n) = \arctan\left(\frac{y_p - (2n+1)}{x_p + 1}\right) + \pi, \tag{11}$$

where $n = 1, 2, \ldots$, we find that

$$f = \begin{cases} f_{\mathrm{in}}, & \theta_2^{(\mathrm{II})}(n+1) < \theta < \theta_1^{(\mathrm{II})}(n) \ \vee \ \theta_2^{(\mathrm{II})}(n) < \theta < \theta_3^{(\mathrm{II})} \ \vee \ \theta_4^{(\mathrm{II})} < \theta < \theta_5^{(\mathrm{II})}(n) \\ & \quad \vee \ \theta_6^{(\mathrm{II})}(n) < \theta < \theta_5^{(\mathrm{II})}(n+1) \\ f_{\mathrm{out}}, & \theta_1^{(\mathrm{II})}(n) < \theta < \theta_2^{(\mathrm{II})}(n) \ \vee \ \theta_3^{(\mathrm{II})} < \theta < \theta_4^{(\mathrm{II})} \ \vee \ \theta_5^{(\mathrm{II})}(n) < \theta < \theta_6^{(\mathrm{II})}(n). \end{cases} \tag{12}$$

In Eq. (12), n division follows as long as $\theta_{1,2}(n) > 3\pi/4$ and $\theta_{5,6}(n) < 5\pi/4$, and terminates at higher n values, where $f = f_{\mathrm{out}}$. Applying symmetry considerations, particle sorting in zone III is similar to the procedure discussed in zone II.

Having determined the distribution function $f(x, y, \boldsymbol{\xi})$, the hydrodynamic fields may be computed using Eq. (7). Given the Gaussian form of f_{in} and f_{out} [see Eq. (6)], all quadratures are carried out analytically, containing sums over the contributions of the sorted θ sections. Relatively concise expressions are found in zone I, where the summation is made over four sections only [see Fig. 2 and Eq. (10)]. The respective expressions are detailed in Appendix A. The counterpart results in zones II and III are more cumbersome, with the number of θ sections to be considered increasing with the distance from the zone I edge (see Fig. 3).

B. Diffuse reflecting walls ($\alpha = 1$)

Setting $\alpha = 1$ in Eq. (5), the state of each gas particle in the channel is determined by its last reflection from any of the corner (free or solid) boundaries. The general solution for the problem is

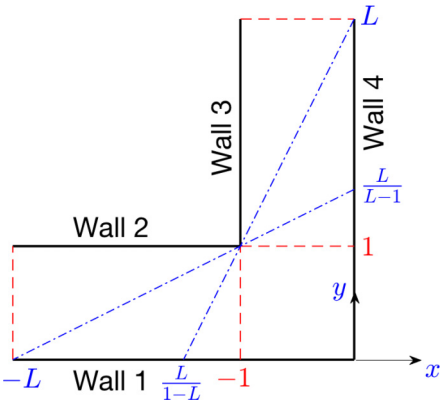

FIG. 4. Analysis of the free-molecular problem in a diffuse-wall setup: the dash-dotted blue lines and dashed $x = -1$ red line divide the $y = 0$ boundary (wall 1) into line segments that are fully obstructed $[-L < x < L/(1-L)]$, partially obstructed $[L/(1-L) < x < -1]$, and fully accessible $[-1 < x < 0]$ to particles arriving from the outlet section $y = L$. Inversely, the $0 < y < 1$, $1 < y < L/(L-1)$ and $L/(L-1) < y < L$ segments of the $x = 0$ boundary (wall 4) pertain to the surface parts that are accessible, partially obstructed and obstructed to particles arriving from the inlet section $x = -L$.

consequently given by

$$f(x, y, \boldsymbol{\xi}) = \frac{\widetilde{\rho}(x_b, y_b)}{(\pi \widetilde{T})^{3/2}} \exp\left[-\frac{\xi^2}{\widetilde{T}}\right], \tag{13}$$

where $\widetilde{T}$ is the prescribed temperature of the emitting boundary, $\widetilde{\rho}(x_b, y_b)$ is an unknown function to be determined, and (x_b, y_b) is the point on the boundary where the particle was last emitted. Given a particle's position (x, y) and its in-plane velocity vector direction θ, its last location at a boundary (x_b, y_b) may be uniquely specified.

Calculation of $\widetilde{\rho}(x_b, y_b)$ is carried out by imposing the impermeability condition,

$$\int_{\boldsymbol{\xi}\cdot\hat{\mathbf{n}}>0} \boldsymbol{\xi}\cdot\hat{\mathbf{n}} f(x_b, y_b, \boldsymbol{\xi}) \mathrm{d}\boldsymbol{\xi} + \int_{\boldsymbol{\xi}\cdot\hat{\mathbf{n}}<0} \boldsymbol{\xi}\cdot\hat{\mathbf{n}} f(x_b, y_b, \boldsymbol{\xi}) \mathrm{d}\boldsymbol{\xi} = 0, \tag{14}$$

along each of the solid corner boundaries. Here, the first and second integrals express the separate contributions of the outgoing and incoming particles to the macroscopic gas velocity normal to the surface, respectively. At a given location, incoming particles may arrive from different boundaries, and their respective contributions should be taken into account accordingly.

Specific implementation of the impermeability condition (14) follows from geometric considerations, taking into account all possible free-flight trajectories of particles that may arrive at a given surface location from other boundaries. Denoting the $y = 0$, $y = 1$, $x = -1$ and $x = 0$ surfaces by wall 1, wall 2, wall 3, and wall 4, respectively, Figure 4 presents the division of walls 1 and 4 into segments that are fully obstructed, partially obstructed, and accessible to particles arriving directly from the outlet of inlet sections. The impermeability condition along these segments should accordingly couple the flux contributions of inlet and outlet particles, which serve as forcing terms in the equations. In the following, we detail the derivation of the impermeability condition along wall 1 to demonstrate our analysis. We then list all other conditions in Appendix B.

Considering the impermeability balance over wall 1 and focusing on the contribution of reflected particles, we substitute Eq. (13) with $\widetilde{\rho}(x_b, y_b) = \widetilde{\rho}_1(x)$ into the first integral in Eq. (14), to obtain

$$\int_{\boldsymbol{\xi}\cdot\hat{\mathbf{n}}>0} \xi_y f(x, 0, \boldsymbol{\xi}) \mathrm{d}\boldsymbol{\xi} = \frac{\widetilde{\rho}_1(x)}{2\sqrt{\pi}}. \tag{15}$$

The contribution of the incoming particles to the flux balance [accounted for by the second integral in Eq. (14)] then varies between the different segments marked in Fig. 4. Along the middle $L/(1-L) < x < -1$ portion, the calculation yields

$$\int_{\boldsymbol{\xi}\cdot\hat{\mathbf{n}}<0} \xi_y f(x,0,\boldsymbol{\xi})\mathrm{d}\boldsymbol{\xi}$$
$$= \frac{1}{4\sqrt{\pi}}\left[\left(\frac{L+x}{\sqrt{(L+x)^2+1}}-1\right)+\int_{\pi+\arctan\left(\frac{-1}{1+x}\right)}^{2\pi-\arctan\left(\frac{1}{L+x}\right)}\widetilde{\rho}_2(x+\cot\theta)\sin\theta\mathrm{d}\theta\right.$$
$$\left.+\int_{\pi}^{\pi-\arctan\left(\frac{L}{x}\right)}\widetilde{\rho}_4(-x\tan\theta)\sin\theta\mathrm{d}\theta-\rho_{\mathrm{out}}\sqrt{T_{\mathrm{out}}}\left(\frac{x+1}{\sqrt{(1+x)^2+1}}-\frac{x}{\sqrt{x^2+L^2}}\right)\right], \quad (16)$$

where the four terms on the RHS mark the contributions of particles arriving from the inlet section, wall 2, wall 4, and part of the outlet, respectively. In deriving Eq. (16), the ξ_z integrals were computed analytically, and the ξ_x and ξ_y quadratures were decomposed into single integrals over the particle trajectory direction θ [see Eq. (8)]. Hereafter, $\widetilde{\rho}_i$ (with $i=2,3,4$) and $\widetilde{\rho}_1$ correspond to the $\widetilde{\rho}$ function appearing in Eq. (13), associated with wall i. Combining Eqs. (15) and (16), we obtain the no-penetration condition over the middle $L/(1-L) < x < -1$ portion of wall 1,

$$\widetilde{\rho}_1(x)+\int_{\pi+\arctan\left(\frac{-1}{1+x}\right)}^{2\pi-\arctan\left(\frac{1}{L+x}\right)}\widetilde{\rho}_2(x+\cot\theta)\sin\theta\mathrm{d}\theta+\int_{\pi}^{\pi-\arctan\left(\frac{L}{x}\right)}\widetilde{\rho}_4(-x\tan\theta)\sin\theta\mathrm{d}\theta$$
$$=\rho_{\mathrm{out}}\sqrt{T_{\mathrm{out}}}\left(\frac{x+1}{\sqrt{(1+x)^2+1}}-\frac{x}{\sqrt{x^2+L^2}}\right)+1-\frac{L+x}{\sqrt{(L+x)^2+1}}, \quad (17)$$

where the outlet and inlet section contributions appear as forcing terms on the RHS. With slight modifications, the flux balance over the remaining parts of wall 1 may be formulated. Along $-L < x < L/(1-L)$, present in channels of length $L > 2$, we find

$$2\widetilde{\rho}_1(x)+\int_{\pi+\arctan\left(\frac{-1}{1+x}\right)}^{2\pi-\arctan\left(\frac{1}{L+x}\right)}\widetilde{\rho}_2(x+\cot\theta)\sin\theta\mathrm{d}\theta+\int_{\pi}^{\pi+\arctan\left(\frac{-1}{1+x}\right)}\widetilde{\rho}_4(-x\tan\theta)\sin\theta\mathrm{d}\theta$$
$$=1-\frac{L+x}{\sqrt{(L+x)^2+1}}, \quad (18)$$

and over $-1 < x < 0$ we obtain

$$2\widetilde{\rho}_1(x)+\int_{2\pi-\arctan\left(\frac{1}{1+x}\right)}^{2\pi-\arctan\left(\frac{1}{L+x}\right)}\widetilde{\rho}_2(x+\cot\theta)\sin\theta\mathrm{d}\theta+\int_{2\pi-\arctan\left(\frac{L}{1+x}\right)}^{2\pi-\arctan\left(\frac{1}{1+x}\right)}\widetilde{\rho}_3(-(1+x)\tan\theta)\sin\theta\mathrm{d}\theta$$
$$+\int_{\pi}^{\pi-\arctan\left(\frac{L}{x}\right)}\widetilde{\rho}_4(-x\tan\theta)\sin\theta\mathrm{d}\theta$$
$$=\rho_{\mathrm{out}}\sqrt{T_{\mathrm{out}}}\left(\frac{x+1}{\sqrt{(1+x)^2+L^2}}-\frac{x}{\sqrt{x^2+L^2}}\right)+1-\frac{L+x}{\sqrt{(L+x)^2+1}}. \quad (19)$$

Similar considerations follow in deriving the impermeability condition along walls 2, 3, and 4, as listed in Appendix B.

Equations (17)–(19) together with (B1)–(B5) form a system of nonhomogeneous flux balances for $\widetilde{\rho}_1(x)$, $\widetilde{\rho}_2(x)$, $\widetilde{\rho}_3(y)$ and $\widetilde{\rho}_4(y)$. In case where the inlet and outlet reservoirs are kept at the same conditions, $\rho_{\mathrm{out}}=T_{\mathrm{out}}=1$, the uniform $\widetilde{\rho}_1(x)=\widetilde{\rho}_2(x)=\widetilde{\rho}_3(y)=\widetilde{\rho}_4(y)=1$ solution is recovered. For any nontrivial combination of ρ_{out} and T_{out}, the equations are solved numerically by discretizing

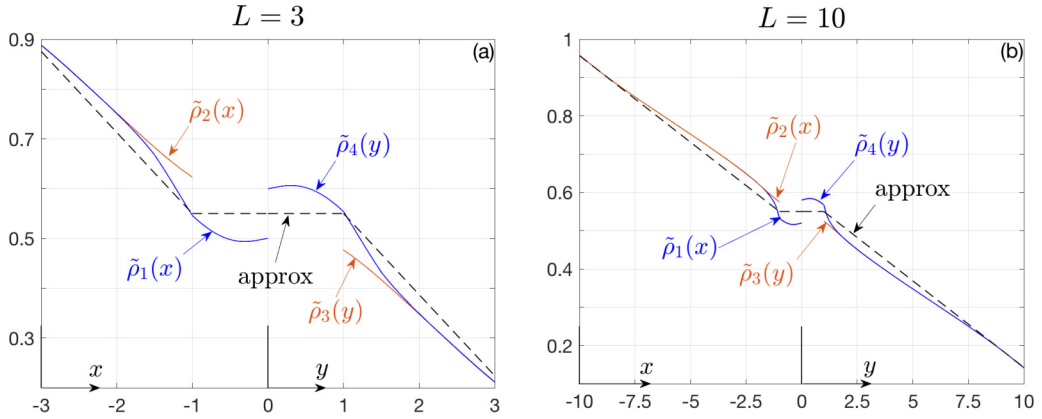

FIG. 5. The free-molecular wall functions $\widetilde{\rho}_1(x)$, $\widetilde{\rho}_2(x)$, $\widetilde{\rho}_3(y)$, and $\widetilde{\rho}_4(y)$ for a density-driven flow ($\rho_{\text{out}} = 0.1$) in a diffuse-wall corner with $L = 3$ [Fig. 5(a)] and $L = 10$ [Fig. 5(b)]. The solid curves show the calculated free-molecular distributions and the dashed lines present their linear approximation.

the fluxes at equally spaced n_w points along the solid boundaries. The integral terms are evaluated using the trapezoidal rule, where the θ intervals are discretized accordingly. The procedure yields a system of n_w linear nonhomogeneous coupled algebraic equations, which are inverted using a MATLAB subroutine. Our calculations indicate that converged results are formed using $n_w \approx 10^3$ discretization points, with a similar number of θ nodes to evaluate the integral terms. This requires a minor computational effort compared with the DSMC calculations described in Sec. IV.

The solid lines in Fig. 5 present the free-molecular $\widetilde{\rho}_i$ distributions calculated in a diffuse-wall corner subject to a density-driven flow with $\rho_{\text{out}} = 0.1$. The left-hand part in each figure shows the x variations of $\widetilde{\rho}_1$ and $\widetilde{\rho}_2$, whereas the right-hand parts depict the y dependencies of $\widetilde{\rho}_3$ and $\widetilde{\rho}_4$. The results are shown for corners of length $L = 3$ [Fig. 5(a)] and $L = 10$ [Fig. 5(b)]. At first, we note the general similarity of all distributions, exhibiting symmetry properties about the origin $(0, 0)$ and inner corner $(-1, 1)$ locations. While $\widetilde{\rho}_2(x)$ and $\widetilde{\rho}_3(y)$ vary nearly linearly along the walls, $\widetilde{\rho}_1(x)$ and $\widetilde{\rho}_4(y)$ become approximately constant through their zone I parts, $-1 < x < 0$ and $0 < y < 1$, respectively. Along $-L < x < -1$, $\widetilde{\rho}_1$ and $\widetilde{\rho}_2$ are nearly identical, similar to $\widetilde{\rho}_3$ and $\widetilde{\rho}_4$ between $1 < y < L$. These observations hold qualitatively for any combination of ρ_{out}, T_{out} and L, and become more effective with increasing L, as seen through comparison between Figs. 5(a) and 5(b).

In line with the above, a linear approximation may be suggested to estimate $\widetilde{\rho}_i$. Admitting the $\rho_{\text{out}}\sqrt{T_{\text{out}}}$ dependence of all outlet forcing terms in Eqs. (17)–(19) and (B1)–(B5), and assuming system symmetry, we put

$$A(L, \rho_{\text{out}}\sqrt{T_{\text{out}}}) = \widetilde{\rho}_1(-L) = \widetilde{\rho}_2(-L),\ B(L, \rho_{\text{out}}\sqrt{T_{\text{out}}}) = \widetilde{\rho}_3(L) = \widetilde{\rho}_4(L)$$
$$\text{and} \quad \widetilde{\rho}_1(-1) = \widetilde{\rho}_2(-1) = \widetilde{\rho}_3(1) = \widetilde{\rho}_4(1) = (A + B)/2, \tag{20}$$

and seek to approximate the fluxes via

$$\widetilde{\rho}_1(-L \leqslant x \leqslant 1) = \widetilde{\rho}_2(x) = \frac{(B - A)(x + 1)}{2(L - 1)} + \frac{A + B}{2},$$
$$\widetilde{\rho}_3(y) = \widetilde{\rho}_4(1 \leqslant y \leqslant L) = \frac{(B - A)(y - 1)}{2(L - 1)} + \frac{A + B}{2}$$
$$\text{and} \quad \widetilde{\rho}_1(-1 < x \leqslant 0) = \widetilde{\rho}_4(0 \leqslant y < 1) = (A + B)/2. \tag{21}$$

To calculate A and B, we substitute Eq. (21) into Eqs. (B1) and (B2) and satisfy the conditions at $(-L, 1)$ and $(-1, L)$. This yields a system of equations for A and B, solved by

$$A = \frac{(1+\rho_{\text{out}}\sqrt{T_{\text{out}}})(L^2-2L+2-\sqrt{L^2-2L+2})-(3+\rho_{\text{out}}\sqrt{T_{\text{out}}})(L-1)\sqrt{L^2-2L+2})}{2(L^2-2L+2-\sqrt{L^2-2L+2})-4(L-1)\sqrt{L^2-2L+2})}$$

$$\text{and} \quad B = 1+\rho_{\text{out}}\sqrt{T_{\text{out}}}-A. \tag{22}$$

The approximate results based on Eqs. (21) and (22) and corresponding to the flow configuration in Fig. 5 are shown by the dashed lines therein, indicating that the estimate improves with increasing L. Advantageously, it provides a useful means to evaluate the mass flow rate through a diffuse corner in a closed form, as discussed in Sec. V.

Once the wall fluxes are known, the probability density function in Eq. (13) is determined and the hydrodynamic fields are evaluated via appropriate quadratures over the velocity space [see Eq. (7)]. At each (x, y) location, the integration averages the contributions of particles arriving from all nonobscured boundaries, in accordance with the channel geometry.

IV. THE DSMC SCHEME

The DSMC method is the most prevalent scheme for analyzing rarefied gas flows [30]. The scheme is known to provide results that converge to the solutions of the Boltzmann equation [31]. In its numerical realization, the physical domain is divided into computational cells and simulation particles are introduced. With each simulation particle representing a large number of real particles, the simulation evolves in time in discrete steps, and particles' motions are divided into free-flight and collision parts. In the former, the particles are translated according to their instantaneous velocity. In the latter, collisions are treated in a stochastic manner, following a chosen collision scheme.

In the present work, we apply the two-dimensional open-source DS2V software [32] to analyze the microcorner problem at large yet finite Knudsen numbers. By doing so, we aim to validate the above free-molecular solution and inspect its breakdown with decreasing Knudsen numbers. The software is frequently used as a reliable tool for computing rarefied gas flows, as in recent investigations on supersonic jet expansion [33], compression corner flow detachment [34], shock-wave detection [35], and microscale reaction-diffusion models [36]. Applying the common "no-time-counter" collision scheme [30], we consider a hard-sphere gas model of molecular interaction. Each simulation was initialized with the microcorner set in a vacuum. Particles were then allowed to enter through the inlet and outlet open boundaries, carrying their respective reservoirs' temperature and density. Outgoing particles were removed from the channel domain and the simulation was followed until a steady state was reached. In line with software settings, the simulation time step was taken $1/3$ of the mean collision time and the mesh was locally adapted such that each computational cell size was considerably lower than the local mean free path. Considering the large Knudsen numbers considered, a number of $\approx 2 \times 10^6$ particles and $\approx 1.5 \times 10^5$ collision cells proved sufficient to ensure reliably converged results. A single run lasted several hours using an Intel 16-core i7 processor machine, marking a computational effort that is far larger than the above-described free-molecular calculation. Additionally, to inspect the validity of Eq. (1) as an approximate inlet and outlet channel condition in the near-free-molecular regime, a larger effort was invested to simulate the channel flow including the reservoirs. The respective calculations and results are discussed in Appendix C.

V. RESULTS

The nondimensional problem stated in Sec. II is governed by the corner side length L, outlet reservoir conditions ρ_{out} and T_{out}, and the gas inlet-based Knudsen number Kn. To present our results, we focus primarily on a corner of side length $L = 3$ and study the effects of outlet reservoir conditions and solid wall accommodation on the free-molecular system behavior. The breakdown

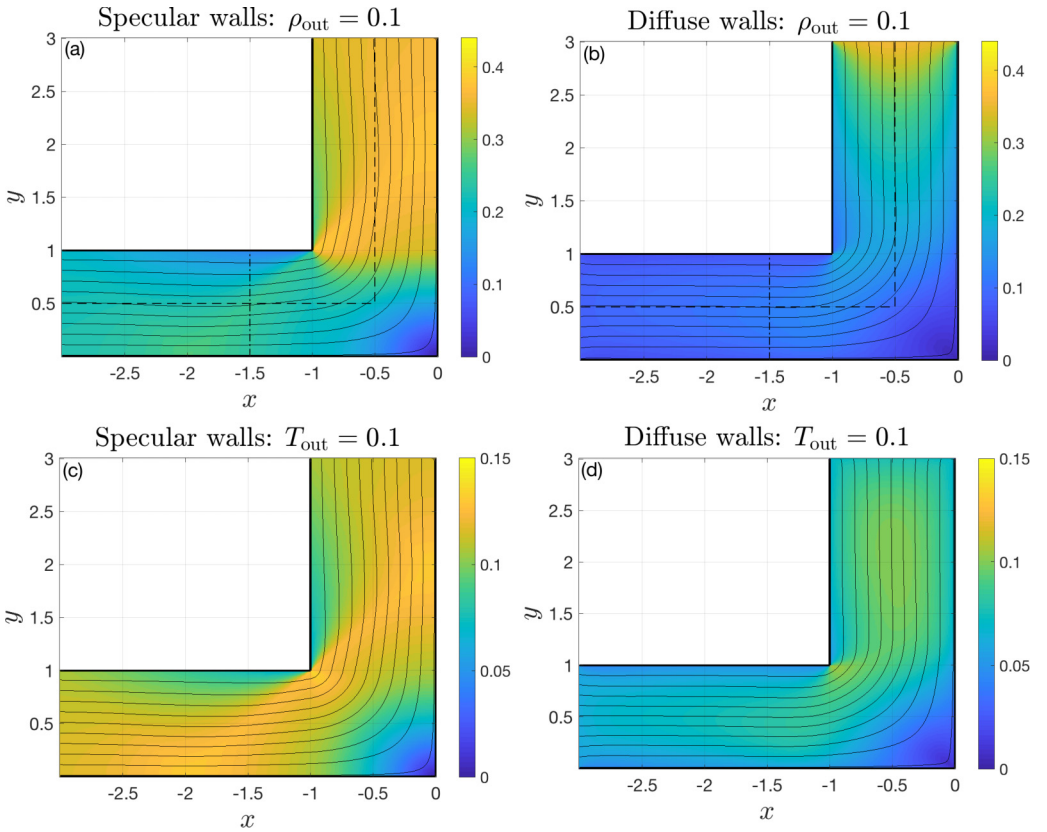

FIG. 6. Velocity magnitude colormaps and streamlines in free-molecular density-driven [Figs. 6(a) and 6(b), $\rho_{out} = 0.1$] and temperature-driven [Figs. 6(c) and 6(d), $T_{out} = 0.1$] corner-flow setups with $L = 3$. Figures 6(a) and 6(c) show results in a specular-wall corner and Figs. 6(b) and 6(d) are for a diffuse-wall configuration. The dashed and dash-dotted lines in Figs. 6(a) and 6(b) mark the corner middle line and $x = -1.5$ section, respectively, along which the results in Fig. 7 are presented.

of the collisionless description with decreasing Kn and the impact of corner size on the mass flow rate through the channel are then discussed.

Figure 6 presents free-molecular velocity magnitude colormaps and flow streamlines in specular [Figs. 6(a) and 6(c)]) and diffuse [Figs. 6(b) and 6(d)] corner setups. Maintaining an outlet-to-inlet pressure ratio of $p_{out}/p_{in} = \rho_{out}T_{out} = 0.1$, density-driven ($\rho_{out} = 0.1$, [Figs. 6(a) and 6(b)]) and temperature-driven [$T_{out} = 0.1$, Figs. 6(c) and 6(d)]) flow setups are considered for comparison. In common with all configurations, we note that the free-molecular flow field is fully attached to the corner walls, even at the low-pressure ratio considered. Free-molecular flow detachment is not observed also when expansion to vacuum ($\rho_{out} = 0$) is inspected. These are in line with previous studies on microcorner flows, indicating that flow separation in this configuration is essentially a low-Knudsen phenomenon [15,18,22]. Invariably, the flow is nearly stagnant close to the origin outer-corner location, while sharp velocity gradients are obtained in the vicinity of its inner $(-1, 1)$ bend.

Comparing the specular- and diffuse-wall setups in Fig. 6, we find significantly higher flow speeds in the former. Indeed, different from the perfectly reflecting specular conditions, the particles' kinetic energy is transmitted to the stationary diffuse-reflecting walls during particle-surface collisions, yielding a reduction in the overall gas velocity magnitude. Additionally, the kinematic

differences between diffuse- and specular-wall emissions, analyzed in Sec. III, are viewed through the sharper flow gradients observed in the latter, particularly in the vicinity of the inner bend $(-1, 1)$ location in Figs. 6(c) and 6(d). Comparing the density- and temperature-driven flows in Figs. 6(a) and 6(b) and Figs. 6(c) and 6(d), respectively, it is viewed that higher flow velocities are induced in the former case. This, in turn, yields higher mass-flow rates in density-driven configurations at a fixed pressure ratio, as discussed below.

To test the validity of our free-molecular solution, Fig. 7 presents a comparison between the ballistic and DSMC results at noninfinite Knudsen numbers. Focusing on a density-driven setup with $\rho_{\text{out}} = 0.1$, the collisionless density and x-velocity fields in Figs. 7(a)–7(d) are inspected along the corner middle-line l, marked by the dashed curve in Figs. 6(a) and 6(b), and combining the $-3 \leqslant x \leqslant -0.5$ (with $y = 0.5$) and $0.5 \leqslant y \leqslant 3$ (with $x = -0.5$) line segments. Figures 7(e) and 7(f) then present counterpart comparisons along the $x = -1.5$ section, denoted by the dash-dotted lines in Figs. 6(a) and 6(b). The results in specular and diffuse-wall corners are shown in Figs. 7(a), 7(c) and 7(e), and 7(b), 7(d) and 7(f), respectively, comparing the collisionless solution (in solid lines) with DSMC predictions at the indicated Knudsen numbers (in symbols).

At first, we note the uniform convergence of all DSMC results to the ballistic limit with increasing Kn, supporting the accuracy of our analysis. Yet, while collisionless conditions are recovered already at $\text{Kn} = 10$ in a diffuse-wall corner, the deviations between DSMC and free-molecular predictions vanish only at $\text{Kn} \approx 100$ in the specular-wall case. Markedly, the free-molecular fields in the specular corner setup appear non-smooth, with sharp gradient changes characterizing all hydrodynamic perturbations. In particular, significant differences between the specular- and diffuse-wall setups are noted in the $x = -0.5$ section results in Figs. 7(e) and 7(f). Here, the diffuse-wall velocity profile is nearly symmetric about $y = 0.5$, whereas a discontinuity in the velocity gradient is seen at about the same y value in the specular case. In line with the results in Fig. 6, the flow speed through the specular-wall corner is considerably larger, reaching $u_x \approx 0.25$, compared to a nearly half value of $u_x \approx 0.125$ in the diffuse-wall case.

To rationalize the non-smoothness in the specular-wall solution, we revert to the free-molecular analysis carried out in Sec. III A. Focusing on the gradient discontinuity in the $x = -1.5$ velocity profile observed in Fig. 7(e) at $y = 0.5$, we make use of Eqs. (11) and (12) to find that, at $(x_p, y_p) = (-1.5, 0.5)$, $\theta_4^{(II)}(1) = \theta_5^{(II)}(1) = 5\pi/4$. Consequently, at $y > 0.5$, there exists a $\theta_4^{(\text{II})} < \theta < \theta_5^{(\text{II})}(1) < 5\pi/4$ interval where $f = f_{\text{in}}$, as illustrated in Fig. 3 for $y = 0.65$. Inversely, at $y < 0.5$, this interval vanishes (as $\theta_{4,5}^{(\text{II})} > 5\pi/4$), and only $\theta_2^{(\text{II})}(1)$ and $\theta_3^{(\text{II})}$ are contained within $3\pi/4 < \theta < 5\pi/4$. This transition, occurring at $y = 0.5$ at the present choice of $x = -1.5$, is the reason for the observed gradient change. All other gradient discontinuities appearing in Figs. 7(a) and 7(c) may be rationalized based on similar considerations. These reflect changes in the sector partition of particles arriving from the inlet or outlet reservoirs at a given position. Comparing with the DSMC results in Figs. 7(a), 7(c), and 7(e), it is noted that even a few molecular collisions are sufficient for significantly smoothing the observed discontinuities. Yet, to some extent, gradient irregularities in a specular-corner setup remain visible through $O(1)$ Knudsen number, as seen in Fig. 7(e).

To assess the accurateness of the inlet and outlet channel conditions stated in Eq. (1) [Eq. (6) in nondimensional form] at near-free-molecular conditions, the problem including reservoirs was simulated, as discussed in Appendix C. The results presented therein (see Fig. 10), comparing our findings in Fig. 7 at finite Knudsen numbers and DSMC predictions where the reservoirs are included, indicate that the effect of reservoirs' flow corrections on the channel flow at $\text{Kn} \gtrsim 3$ is minor. This warrants our application of Eq. (1) as a viable approximation for modeling the microcorner flow problem at large Knudsen numbers.

Microchannel flow performance is primarily measured through its mass flow rate at given flow conditions. Here, we examine the impact of the channel bend on its flow permeability. Mass

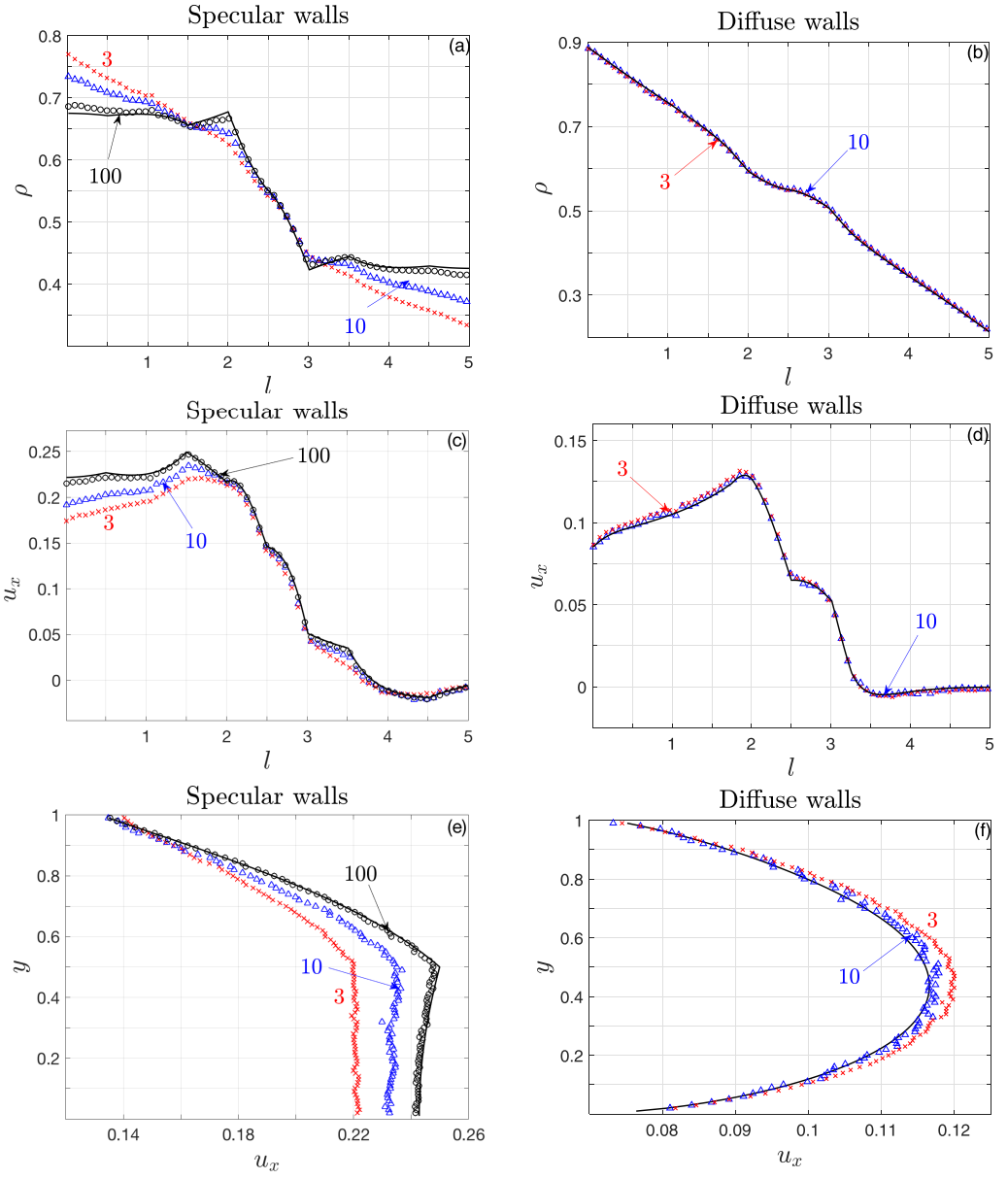

FIG. 7. Comparison between free-molecular (solid lines) and DSMC predictions (symbols) for density-driven flow ($\rho_{\text{out}} = 0.1$) in diffuse [Figs. 7(a), 7(c), and 7(e)] and specular [Figs. 7(b), 7(d), and 7(f)] wall corners with $L = 3$. Figures 7(a)–7(d) show variations of the density [Figs. 7(a) and 7(b)] and x-velocity [Figs. 7(c) and 7(d)] fields along the corner middle line, marked by the dashed curves in Figs. 6(a) and 6(b). Figures 7(e) and 7(f) present y variations of the x-velocity profile along $x = -1.5$, depicted by the dash-dotted lines in Figs. 6(a) and 6(b). In all parts, the numbers refer to the values of the Knudsen number assigned in respective DSMC calculations.

conservation considerations impose that the flow rate is constant along all corner sections,

$$\dot{m} = \int_0^1 [\rho u_x]_{(x\leqslant -1,y)} \mathrm{d}y = \int_{-1}^0 [\rho u_y]_{(x,y\geqslant 1)} \mathrm{d}x, \tag{23}$$

and it is therefore sufficient to calculate its value at a single section. As a reference, we consider a specular-reflecting straight channel setup at free-molecular conditions, where it is established that [13]

$$\dot{m}^{(\mathrm{spec,straight})} = \frac{1}{2\sqrt{\pi}}(1 - \rho_{\mathrm{out}}\sqrt{T_{\mathrm{out}}}). \tag{24}$$

The expression in Eq. (24) is independent of the channel length and is identical to the mass flow rate through an infinitely thin slit at the same inlet and outlet conditions [37]. Advantageously, and based on the results in Appendix A, the mass flow rate through a specular wall right-angled corner may be calculated in a closed form. Substituting the expression for ρu_x in Eq. (A2) into Eq. (23) and taking $x = -1$, we find

$$\dot{m}^{(\mathrm{spec,bend})} = \int_0^1 [\rho u_x]_{(x=-1,y)}\mathrm{d}y = \frac{(1 - \rho_{\mathrm{out}}\sqrt{T_{\mathrm{out}}})(2 - \sqrt{2})}{2\sqrt{\pi}}, \tag{25}$$

yielding the same linear and square-root dependencies on ρ_{out} and T_{out}, respectively, as in Eq. (24) for a straight channel. These are in line with the higher x velocities obtained in the density-driven configuration, as illustrated in Figs. 6 and 7. Yet, more importantly, we find that the mass flow rate through a specular right-angled corner is reduced by a factor of

$$\dot{m}^{(\mathrm{spec,bend})}/\dot{m}^{(\mathrm{spec,straight})} = 2 - \sqrt{2} \approx 0.59, \tag{26}$$

compared with a straight channel. This reduction of more than 40% characterizes the effect of channel bend on its permeability. To the best of our knowledge, this result has not been reported hitherto.

While the corner size has no effect on its mass flow transfer in a specular-reflecting setup, it does alter the result for diffuse scattering walls. Different from the specular setup, a particle entering the corner from any of the reservoirs may not leave the channel when diffuse conditions are imposed. This results in reductions in both gas flow speed, as reflected by the results in Figs. 6 and 7, and the total mass flow rate, manifesting the diminished permeability of a diffuse channel. Previous works have considered the effects of channel size and boundary conditions on free-molecular gas transfer in straight channels, based on Clausing's integral equation [38] and follow-up approximations [39,40]. The particular impact of channel bend on the free-molecular flow rate in a diffuse-reflecting configuration is analyzed below.

Following the free-molecular solution presented in Sec. III B, the mass flow rate through a diffuse-wall corner may be evaluated numerically. Additionally, based on the linear approximation carried out for the wall functions $\widetilde{\rho}_i$ [see Fig. 5 *et seq.*], $\dot{m}$ may be more efficiently estimated. To this end, we focus on the inlet $x = -L$ corner section, and substitute Eqs. (20)–(22) into Eq. (13) and then into (7), to obtain

$$\begin{aligned}[\rho u_x]_{(x=-L,y)} = \frac{1}{4\sqrt{\pi}}\Bigg[&2 - 2A + \frac{(A-B)\sqrt{(1-y)^2+L^2}}{2(L-1)} + \frac{(B-A)((1-y)^2+L(L-1))}{2(L-1)\sqrt{(1-y)^2+(L-1)^2}} \\ &+ \frac{(B-A)(1-y)}{4(L-1)}\ln\left(\frac{\sqrt{(1-y)^2+(L-1)^2}-L+1}{\sqrt{(1-y)^2+(L-1)^2}+L-1}\right) \\ &+ \frac{(A-B)y}{4(L-1)}\ln\left(\frac{\sqrt{y^2+(L-1)^2}+L-1}{\sqrt{y^2+(L-1)^2}-L+1}\right)\Bigg].\end{aligned} \tag{27}$$

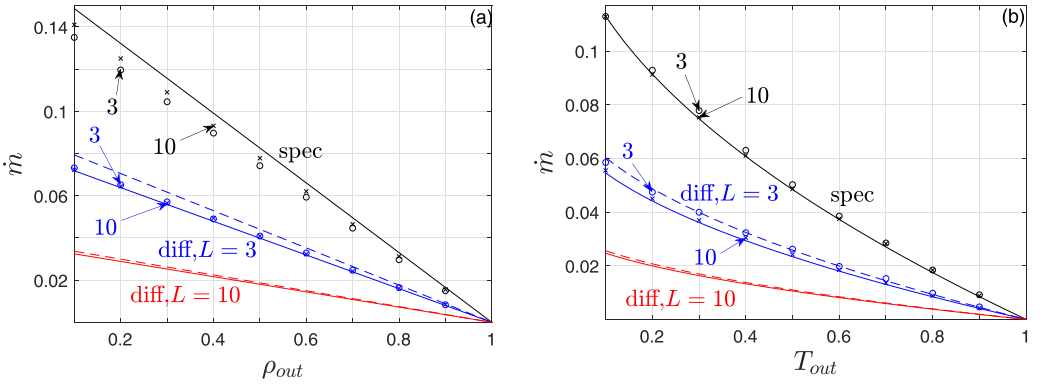

FIG. 8. Variations of the mass flow rate with outlet reservoir conditions in density-driven [Fig. 8(a)] and temperature-driven [Fig. 8(b)] corner flows. In each part, the solid lines show the free-molecular results and the symbols present DSMC predictions at the indicated values of the Knudsen number. The black and blue notations mark data in specular- and diffuse-wall corners with $L = 3$, respectively. The red marks present results in a diffuse-wall corner with $L = 10$. The dashed blue and dashed red curves show the counterpart free-molecular mass-flow-rate variations based on the linear approximation in Eq. (28) in a diffuse-wall corner with $L = 3$ and $L = 10$, respectively.

Substituting Eq. (27) into Eq. (23) and integrating, we obtain a closed-form approximation for the mass flow rate through a diffuse-wall corner, namely

$$\dot{m}^{(\mathrm{diff,bend})} \approx \frac{1}{4\sqrt{\pi}}\Bigg[2+\frac{(B-A)L-3A-B}{2}+\frac{(A-B)\sqrt{L^2+1}+(A-B)(2L-3)\sqrt{L^2-2L+2}}{4(L-1)}$$
$$+\frac{(B-A)(L+1)\mathrm{asinh}\left(\frac{1}{L-1}\right)}{4}+\frac{(A-B)L^2\mathrm{asinh}\left(\frac{1}{L}\right)}{4(L-1)}+\frac{(B-A)\ln\left(\frac{\sqrt{L^2-2L+2}-L+1}{\sqrt{L^2-2L+2}+L-1}\right)}{8(L-1)}$$
$$+\frac{(A-B)\ln(2L^2-4L+3+2(L-1)\sqrt{L^2-2L+2})}{8(L-1)}\Bigg]. \tag{28}$$

Compared with the channel-size-independent specular-corner expression in Eq. (25), the complex L dependence of the diffuse-corner mass flow rate is indicated. The dependence of $\dot{m}^{(\mathrm{diff,bend})}$ on the outlet reservoir conditions ρ_{out} and T_{out} is contained through the values of A and B specified in Eq. (22). The expression turns singular for $L \to 1$, corresponding to a degenerated case where zones II and III vanish (see Fig. 1). As demonstrated below, the accuracy of the approximation improves with increasing L.

The results for the corner mass flow rate are presented in Fig. 8. The variations of $\dot{m}$ with ρ_{out} and T_{out} are shown in Figs. 8(a) and 8(b), respectively, with each comparing the mass flow rate between specular- and diffuse-wall configurations. The L-independent free-molecular predictions in a specular-wall corner are depicted by the solid black lines. The ballistic mass flow rate in a diffuse-wall setup is presented for $L = 3$ (in blue) and $L = 10$ (in red) corners. Here, the solid lines show the free-molecular numerical results and the dashed curves mark their counterpart linear-based approximations. DSMC predictions are marked by the crosses and circles notations at the indicated $\mathrm{Kn} = 10$ and $\mathrm{Kn} = 3$ values, respectively.

We note that all mass flow rates decrease monotonically with decreasing pressure differences between the reservoirs and vanish for $p_{\mathrm{out}} = 1$. In line with Eq. (25), the linear ρ_{out} and nonlinear (square-root) T_{out} declines in $\dot{m}$ are reflected in Figs. 8(a) and 8(b), respectively. The mass flow rate in a diffuse-wall corner is invariably smaller than in a specular-wall configuration and further

reduces with increasing corner size. The latter results from the larger amount of gas kinetic energy transferred to the diffuse corner walls along a longer channel. The collisionless results are well supported by DSMC predictions at $\mathrm{Kn} \gtrsim O(1)$ in the diffuse-wall case. In line with the results in Appendix C, a similar agreement (within 1% deviations) was obtained between the present DSMC-calculated flow rates at finite $\mathrm{Kn} \gtrsim 3$ and their counterpart values computed where reservoir flow is simulated. Following the comparison in Fig. 7 and subsequent discussion, the convergence to the ballistic limit is somewhat slower in the specular-corner case, yet achieved uniformly at large enough Knudsen numbers. Remarkably, the closed-form expression in Eq. (28), marked by the dashed curves, forms an effective approximation in quantifying the diffuse-wall flow rate. In line with the results in Fig. 5, the linear-based approximation matches better with the numerical solution with increasing corner size. Specifically, a maximum deviation of $\approx 8\%$ is found for a corner with $L = 3$, reducing to a discrepancy of $\lesssim 3\%$ for $L = 10$.

VI. CONCLUSIONS

We investigated the two-dimensional steady flow of a highly rarefied gas through a right-angled channel corner element. Driven by an external pressure gradient, the free-molecular regime was analyzed for both diffuse and specular reflecting surfaces, and the solutions were validated using DSMC calculations at finite Knudsen numbers. Imposing the driving pressure gradient through prescribed differences between the density and temperature of gas reservoirs connected to the channel inlet and outlet, the results for the density- and temperature-drop-driven flows were analyzed and contrasted. The characteristic differences between the diffuse- and specular-wall-induced flow fields, indicating sharper flow gradients and higher flow velocities in the latter, were rationalized. Closed-form expressions for the mass flow rate through the corner were derived, indicating a decrease of more than 40% in its mass transfer permeability due to the bend, compared with a straight channel setup.

Perhaps the main contribution of the present work is in providing an analytical description for the free-molecular gas flow in a right-angled corner, which is found effective through $O(1)$ Knudsen numbers. Apart from being prominently efficient compared with existing numerical schemes, the obtained results assist in shedding light on the kinematics and physical mechanisms governing gas flow through curved microchannel geometries. A desirable yet nontrivial extension of the current study would be a counterpart investigation of microchannel gas flows through non-right-angled curved configurations, yielding different results for the channel mass flow rate. Additionally, more complex double-corner canonical setups, such as those considered in Refs. [21,22], may be inspected. These, together with a rigorous asymptotic study on the effect of slight molecular collisions on micro-corner channel flows, constitute topics for future efforts.

ACKNOWLEDGMENTS

This research was supported by the Israel Science Foundation (Grant No. 412/21).

APPENDIX A: THE FREE-MOLECULAR HYDRODYNAMIC FIELDS IN ZONE I FOR A SPECULAR-WALL CORNER

Substituting Eq. (10) into Eq. (7) and carrying out the integrations, we find, for all (x, y) locations within zone I of a specular-wall corner,

$$\rho = \rho_{\mathrm{out}} + \frac{1-\rho_{\mathrm{out}}}{2\pi}\left[\arctan\left(\frac{y+1}{x+1}\right) + \arctan\left(\frac{y-1}{x-1}\right) - \arctan\left(\frac{y-1}{x+1}\right) - \arctan\left(\frac{y+1}{x-1}\right)\right], \tag{A1}$$

$$u_x = \frac{1-\rho_{\rm out}\sqrt{T_{\rm out}}}{4\rho\sqrt{\pi}}\left[\frac{y+1}{\sqrt{(y+1)^2+(x+1)^2}}+\frac{y-1}{\sqrt{(y-1)^2+(x-1)^2}}\right.$$
$$\left.-\frac{y-1}{\sqrt{(y-1)^2+(x+1)^2}}-\frac{y+1}{\sqrt{(y+1)^2+(x-1)^2}}\right], \tag{A2}$$

$$u_y = \frac{1-\rho_{\rm out}\sqrt{T_{\rm out}}}{4\rho\sqrt{\pi}}\left[\frac{x+1}{\sqrt{(y-1)^2+(x+1)^2}}-\frac{x+1}{\sqrt{(y+1)^2+(x+1)^2}}\right.$$
$$\left.-\frac{x-1}{\sqrt{(y-1)^2+(x-1)^2}}+\frac{x-1}{\sqrt{(y+1)^2+(x-1)^2}}\right], \tag{A3}$$

$$P_{xx} = \rho_{\rm out}T_{\rm out}+\frac{1-\rho_{\rm out}T_{\rm out}}{2\pi}\left[\frac{(y+1)(x+1)}{(y+1)^2+(x+1)^2}+\arctan\left(\frac{y+1}{x+1}\right)+\frac{(y-1)(x-1)}{(y-1)^2+(x-1)^2}\right.$$
$$+\arctan\left(\frac{y-1}{x-1}\right)-\frac{(y-1)(x+1)}{(y-1)^2+(x+1)^2}-\arctan\left(\frac{y-1}{x+1}\right)-\frac{(y+1)(x-1)}{(y+1)^2+(x-1)^2}$$
$$\left.-\arctan\left(\frac{y+1}{x-1}\right)\right]-2\rho u_x^2, \tag{A4}$$

$$P_{yy} = \rho_{\rm out}T_{\rm out}+\frac{1-\rho_{\rm out}T_{\rm out}}{2\pi}\left[\arctan\left(\frac{y+1}{x+1}\right)-\frac{(y+1)(x+1)}{(y+1)^2+(x+1)^2}-\frac{(y-1)(x-1)}{(y-1)^2+(x-1)^2}\right.$$
$$+\arctan\left(\frac{y-1}{x-1}\right)+\frac{(y-1)(x+1)}{(y-1)^2+(x+1)^2}-\arctan\left(\frac{y-1}{x+1}\right)+\frac{(y+1)(x-1)}{(y+1)^2+(x-1)^2}$$
$$\left.-\arctan\left(\frac{y+1}{x-1}\right)\right]-2\rho u_y^2, \tag{A5}$$

and

$$P_{zz} = \rho_{\rm out}T_{\rm out}+\frac{1-\rho_{\rm out}T_{\rm out}}{2\pi}\left[\arctan\left(\frac{y+1}{x+1}\right)+\arctan\left(\frac{y-1}{x-1}\right)-\arctan\left(\frac{y-1}{x+1}\right)\right.$$
$$\left.-\arctan\left(\frac{y+1}{x-1}\right)\right]. \tag{A6}$$

APPENDIX B: THE IMPERMEABILITY CONDITIONS IN A DIFFUSE-WALL CORNER AT FREE-MOLECULAR CONDITIONS

Following similar arguments to those described in Sec. III B, the impermeability conditions over walls 2, 3, and 4 are derived. Skipping the technical details for brevity, the no-penetration condition over wall 2 ($-L < x < -1$, $y = 1$) is given by

$$-2\widetilde{\rho}_2(x)+\int_{2\pi+\arctan(\frac{1}{L+x})}^{3\pi+\arctan(\frac{1}{x})}\widetilde{\rho}_1(x-\cot\theta)\sin\theta\,{\rm d}\theta+\int_{3\pi+\arctan(\frac{1}{x})}^{3\pi}\widetilde{\rho}_4(1-x\tan\theta)\sin\theta\,{\rm d}\theta$$
$$=\frac{L+x}{\sqrt{(L+x)^2+1}}-1, \tag{B1}$$

whereas over wall 3 ($x = -1, 1 < y < L$)

$$2\widetilde{\rho}_3(x) + \int_{\pi/2}^{\pi/2+\arctan(\frac{1}{y})} \widetilde{\rho}_1(-1 - y\cot\theta)\cos\theta \mathrm{d}\theta + \int_{\pi/2+\arctan(\frac{1}{y})}^{\pi+\arctan(L-y)} \widetilde{\rho}_4(y + \tan\theta)\cos\theta \mathrm{d}\theta$$
$$= \rho_{\text{out}}\sqrt{T_{\text{out}}}\left(1 - \frac{L-y}{\sqrt{(L-y)^2+1}}\right). \tag{B2}$$

Similarly to the discussion of wall 1 in Sec. III B, wall 4 ($x = 0, 0 < y < L$) is divided into three sections. Along $L/(L-1) < y < L$ (present for corners of side length $L > 2$) we obtain

$$-2\widetilde{\rho}_4(x) + \int_{2\pi+\arctan(y-1)}^{5\pi/2} \widetilde{\rho}_1(-y\cot\theta)\cos\theta \mathrm{d}\theta + \int_{3\pi/2+\arctan(\frac{1}{L-y})}^{2\pi+\arctan(y-1)} \widetilde{\rho}_3(y - \tan\theta)\cos\theta \mathrm{d}\theta$$
$$= \rho_{\text{out}}\sqrt{T_{\text{out}}}\left(\frac{L-y}{\sqrt{(L-y)^2+1}} - 1\right), \tag{B3}$$

whereas along $1 < y < L/(L-1)$

$$-2\widetilde{\rho}_4(x) + \int_{2\pi+\arctan(\frac{y}{L})}^{5\pi/2} \widetilde{\rho}_1(-y\cot\theta)\cos\theta \mathrm{d}\theta + \int_{3\pi/2+\arctan(\frac{1}{L-y})}^{2\pi+\arctan(y-1)} \widetilde{\rho}_3(y - \tan\theta)\cos\theta \mathrm{d}\theta$$
$$= \rho_{\text{out}}\sqrt{T_{\text{out}}}\left(\frac{L-y}{\sqrt{(L-y)^2+1}} - 1\right) + \frac{y-1}{\sqrt{1+(y-1)^2}} - \frac{y}{\sqrt{L^2+y^2}}, \tag{B4}$$

and for $0 < y < 1$

$$-2\widetilde{\rho}_4(x) + \int_{2\pi+\arctan(\frac{y}{L})}^{5\pi/2} \widetilde{\rho}_1(-y\cot\theta)\cos\theta \mathrm{d}\theta + \int_{2\pi+\arctan(y-1)}^{2\pi+\arctan(\frac{y-1}{L})} \widetilde{\rho}_2((1-y)\cot\theta)\cos\theta \mathrm{d}\theta$$
$$+ \int_{3\pi/2+\arctan(\frac{1}{L-y})}^{2\pi+\arctan(y-1)} \widetilde{\rho}_3(y - \tan\theta)\cos\theta \mathrm{d}\theta$$
$$= \rho_{\text{out}}\sqrt{T_{\text{out}}}\left(\frac{L-y}{\sqrt{(L-y)^2+1}} - 1\right) + \frac{y-1}{\sqrt{(y-1)^2+L^2}} - \frac{y}{\sqrt{L^2+y^2}}. \tag{B5}$$

APPENDIX C: THE EFFECT OF CHANNEL RESERVOIRS ON THE CHANNEL FLOW FIELD

To assess the accurateness of the inlet and outlet channel conditions stated in Eq. (1) at near-free-molecular conditions, the problem including reservoirs was analyzed using DSMC calculations. A schematic of the simulated setup is presented in Fig. 9, where the inlet and outlet reservoirs of dimensions $L_R^* \times H_R^*$ confine the right-angled corner introduced in Fig. 1. Following previous studies on reservoir-confined problems [28], the reservoirs' walls attached to the channel ends, marked by the thin solid lines, were modeled using the same conditions as the corner boundaries (specular or diffuse). The thin dashed lines, marking the reservoirs' side and far-end surfaces, were set as open boundaries.

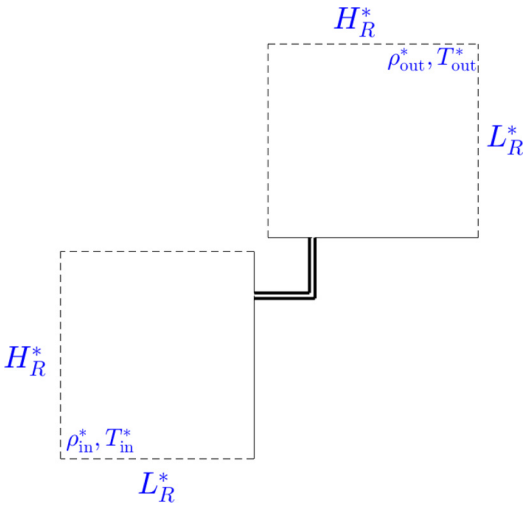

FIG. 9. Schematic of the problem with reservoirs. The right-angled micro-corner introduced in Fig. 1 is placed between the inlet and outlet reservoirs of dimensions $L_R^* \times H_R^*$, which are set with far-field densities ρ_{in}^* and ρ_{out}^*, and temperatures T_{in}^* and T_{out}^*, respectively. The reservoir walls attached to the channel ends and marked by the thin solid lines are modeled using the same conditions as the corner boundaries (specular or diffuse). The thin dashed lines, marking the reservoirs' sides and far-end surfaces, are open boundaries.

As in the simulation procedure in the absence of reservoirs (see Sec. IV), the system with reservoirs was initially set in a vacuum. Then, starting at time $t = 0$, particles were allowed to enter the domain through the reservoirs' open surfaces (see Fig. 9), assigned with their respective Maxwellian distributions at the entrance. The system evolution was followed in time, with particles intermolecular collisions and surface interactions modeled. Particles exiting the reservoir open boundaries were removed from the domain and the simulation continued until a steady state was obtained. The reservoirs' dimensions were chosen large enough so that the entire effect of molecular interactions between particles leaving and entering the microcorner through its inlet and outlet sections was captured. Specifically, we considered square-form reservoirs of sizes $L_R = H_R = 50$ and $L_R = H_R = 20$. Our calculations indicate that at the large $\text{Kn} \gtrsim 3$ values considered, each reservoir remains nearly unaffected by collisions with particles entering from the channel, apart from the close vicinity of the entrance section. Inevitably, the simulation of the problem including reservoirs required considerably larger computational effort, with the number of particles and collision cells being one to two orders of magnitude larger than those stated in Sec. IV. As a result, each calculation lasted several days using our computational resources.

A comparison between DSMC-calculated results for setups with and without reservoirs is presented in Fig. 10. To relate to the results in Fig. 7, Fig. 10 shows the effect of the reservoirs on the x-velocity field calculated along an $L = 3$ corner middle line in the same case of a density-driven flow with $\rho_{\text{out}} = 0.1$. DSMC predictions are presented for $\text{Kn} = 10$ in Figs. 10(a) and 10(b), and for $\text{Kn} = 3$ in Figs. 10(c) and 10(d), for specular- and diffuse-wall corners. In each figure, the results are compared between a setup with no reservoirs (as presented in Fig. 7) and squared-reservoir configurations of sizes $L_R = H_R = 20$ and $L_R = H_R = 50$. The free-molecular solution is marked by the solid lines for reference. Notably, DSMC results for systems with and without reservoirs closely agree in all cases. This indicates that the impact of the end effect, originating from the interactions of particles inside the reservoirs prior to their entrance to the channel, is negligible at the large Knudsen numbers considered. The discrepancies between the free-molecular and DSMC results in Fig. 10 are attributed, as in Fig. 7, to the impact of molecular collisions inside the channel, being equally simulated in DSMC calculations with and without the reservoirs. The results in Fig. 10

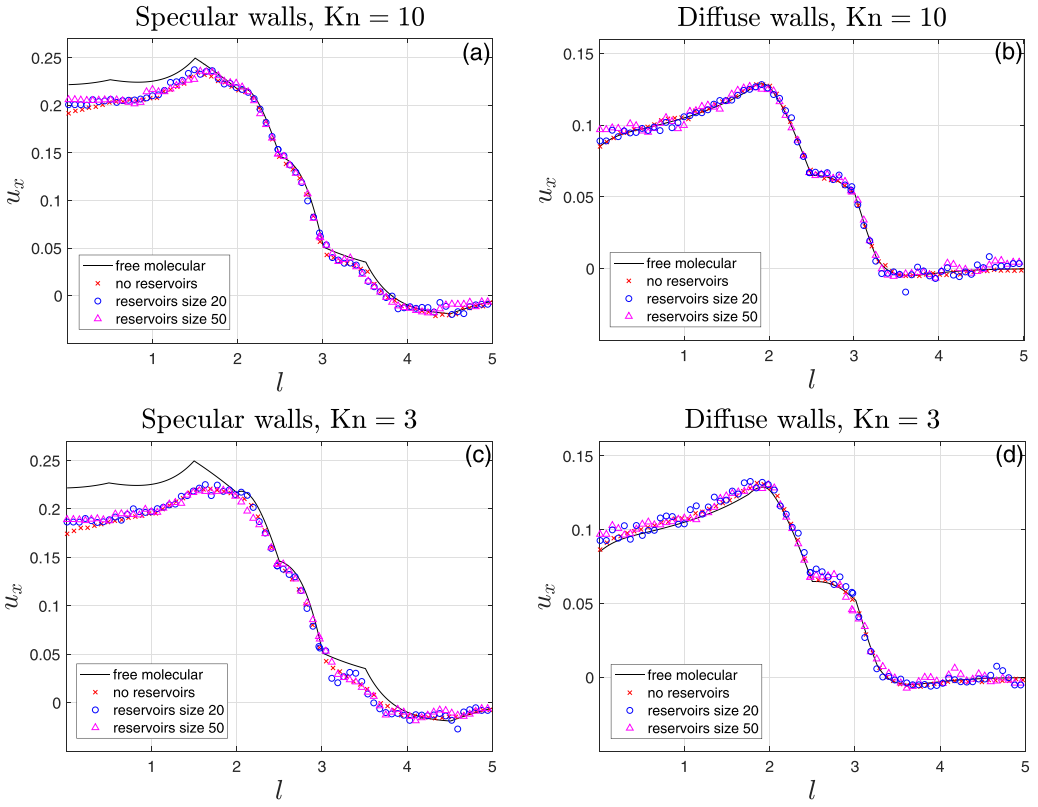

FIG. 10. Effect of the reservoirs on the x-velocity field obtained along an $L = 3$ corner middle line. The results present DSMC calculations at Kn $= 10$ [(a) and (b)] and Kn $= 3$ [(c) and (d)] for specular [(a) and (c)] and diffuse [(b) and (d)] wall corners. In each figure, the results are compared between a setup with no reservoirs (red crosses) and configurations with reservoirs of sizes $L_R = H_R = 20$ (blue circles) and $L_R = H_R = 50$ (magenta triangles). The free-molecular solution is marked by the solid lines for reference. The results in all cases are for density-driven flow setup with $\rho_{\text{out}} = 0.1$.

therefore warrant our application of Eq. (1) as a viable means for modeling the problem at high rarefaction rates, which, in turn, significantly simplifies the analysis.

[1] G. Karniadakis, A. Beskok, and N. Aluru, *Microflows and Nanoflows: Fundamentals and Simulation* (Springer, New York, 2005).

[2] S. Kandlikar, D. Li, M. King, S. Garimella, and S. Colin, *Heat Transfer and Fluid Flow in Minichannels and Microchannels* (Elsevier, Oxford, UK, 2006).

[3] T. Thorsen, S. Maerkl, and S. Quake, Microfluidic large-scale integration, Science **298**, 580 (2002).

[4] F. Sharipov and I. A. Graur, Rarefied gas flow through a zigzag channel, Vacuum **86**, 1778 (2012).

[5] S. Naris, C. Tantos, and D. Valougeorgis, Kinetic modeling of a tapered holweck pump, Vacuum **109**, 341 (2014).

[6] I. Graur, T. Veltzke, J. G. Meolans, M. T. Ho, and J. Thoming, The gas flow diode effect: Theoretical and experimental analysis of moderately rarefied gas flows through a microchannel with varying cross section, Microfluidics and Nanofluidics **18**, 391 (2015).

[7] V. Hemadri, V. Parade, and A. A. U. Bhandarkar, Investigation of rarefied gas flow in microchannels of non-uniform cross section, Phys. Fluids **28**, 022007 (2016).
[8] G. Tatsios, G. L. Quesada, M. Rojas-Cardenas, L. Baldas, S. Colin, and D. Valougeorgis, Computational investigation and parametrization of the pumping effect in temperature-driven flows through long tapered channels, Microfluidics and Nanofluidics **21**, 99 (2017).
[9] A. Agrawal, L. Djenidi, and R. A. Antonia, Simulation of gas flow in microchannels with a sudden expansion or contraction, J. Fluid Mech. **530**, 135 (2005).
[10] Z. Hong, C. Zhen, and C. Yang, Fluid dynamics and heat transfer analysis of three dimensional microchannel flows with microstructures, Numerical Heat Transfer A **54**, 293 (2008).
[11] A. Gat, I. Frankel, and D. Weihs, Gas flows through constricted shallow micro-channels, J. Fluid Mech. **602**, 427 (2008).
[12] V. Varade, A. Agrawal, and A. M. Paradeep, Behaviour of rarefied gas flow near the junction of a suddenly expanding tube, J. Fluid Mech. **739**, 363 (2014).
[13] A. Manela and L. Gibelli, Free-molecular and near-free-molecular gas flows over backward facing steps, J. Fluid Mech. **889**, A22 (2020).
[14] D. Ben-Adva, D. G. Tatsios, and A. Manela, Kinetic description of flow detachment at a smooth microstep: the near-free-molecular regime, Theor. Comput. Fluid Dyna. **39**, 11 (2025).
[15] A. Taassob, A. Bordbar, S. Kheirandish, A. Zarnaghsh, R. Kamali, and A. S. Rana, A review of rarefied gas flow in irregular micro/nanochannels, J. Micromech. Microeng. **31**, 113002 (2021).
[16] S. Y. K. Lee, M. Wong, and Y. Zohar, Gas flow in microchannels with bends, J. Micromech. Microeng. **11**, 635 (2001).
[17] R. Raju and S. Roy, Hydrodynamic model for microscale flows in a channel with two 90° bends, J. Fluids Eng. **126**, 489 (2004).
[18] V. Varade, A. Agrawal, S. Prabhu, and A. Pradeep, Early onset of flow separation with rarefied gas flowing in a 90° bend tube, Exp. Therm Fluid Sci. **66**, 221 (2015).
[19] H. S. Singh, P. M. V. Subbarao, and S. Dhanekar, Experimental and numerical study of gas flow through microchannel with 90° bends, J. Micromech. Microeng. **32**, 095003 (2022).
[20] C. White, M. K. Borg, T. J. Scanlon, and J. M. Reese, A DSMC investigation of gas flows in microchannels with bends, Computers & Fluids **71**, 261 (2013).
[21] W. Liu, G. Tang, W. Su, L. Wu, and Y. Zhang, Rarefaction throttling effect: Influence of the bend in micro-channel gaseous flow, Phys. Fluids **30**, 082002 (2018).
[22] M. T. Ho, J. Li, W. Su, L. Wu, M. K. Borg, Z. Li, and Y. Zhang, Rarefied flow separation in microchannel with bends, J. Fluid Mech. **901**, A26 (2020).
[23] O. Rovenskaya, Computational study of 3D rarefied gas flow in microchannel with 90 bend, Eur. J. Mech. B Fluids **59**, 7 (2016).
[24] N. Kulakarni, K. Shterev, and S. Stefanov, Effects of finite distance between a pair of opposite transversal dimensions in microchannel configurations: DSMC analysis in transitional regime, Int. J. Heat Mass Transf. **85**, 568 (2015).
[25] S. Pantazis, D. Valougeorgis, and F. Sharipov, End corrections for rarefied gas flows through capillaries of finite length, Vacuum **97**, 26 (2013).
[26] Z. Shi, Y. Zhao, W. Su, and L. Wu, Highly rarefied gas flows in rough channels of finite length, Advances in Aerodynamics **5**, 27 (2023).
[27] J. Qian, H. Wu, and F. Wang, A generalized Knudsen theory for gas transport with specular and diffuse reflections, Nat. Commun. **14**, 7386 (2023).
[28] O. Sazhin, Gas outflow into vacuum over a forward- and backward-facing step in a wide range of rarefaction, Int. J. Heat Mass Transf. **179**, 121666 (2021).
[29] Y. Sone, *Molecular Gas Dynamics: Theory, Techniques, and Applications* (Birkhäuser Boston, 2007).
[30] G. Bird, *Molecular Gas Dynamics and the Direct Simulation of Gas Flows* (Oxford University Press, Clarendon, 1994).
[31] W. Wagner, A convergence proof for Bird's direct simulation Monte Carlo method for the Boltzmann equation, J. Stat. Phys. **66**, 1011 (1992).

[32] Visual DSMC program for two-dimensional flows. In: The DS2V program user's guide version 4.5, http://gab.com.au.
[33] M. Patel, Flow characterization of supersonic gas jets: Experiments and simulations, Vacuum **192**, 110440 (2021).
[34] X. Li, Y. Yu, and L. Bao, Theory-based prediction of separation angle and peak pressure for laminar separated hypersonic compression corner flows, Phys. Fluids **33**, 086106 (2021).
[35] L. Kovacs, P. Passaggaia, N. Mazellier, and V. Lago, Detection method for shock-waves in viscous flows, Exp. Fluids **63**, 11 (2022).
[36] S. L. Zhang and Z. H. Wang, Theoretical modelling of non-equilibrium reaction-diffusion of rarefied gas on a wall with microscale roughness, J. Fluid Mech. **965**, A21 (2023).
[37] C. Cercignani, *Theory and Application of the Boltzmann Equation* (Scottish Academic Press, Edinburgh, 1975).
[38] P. Clausing, Über die strömung sehr verdünntern case durch röhren von beliebiger länge, Annalen der Physik **404**, 961 (1932).
[39] A. Berman, Free molecule transmission probabilities, J. Appl. Phys. **36**, 3356 (1965).
[40] J. Helmer, Solution of Clausing's integral equation for molecular flow, J. Vac. Sci. Technol. **4**, 360 (1967).